On-Surface Boronation of Porphyrin into A Molecular Dipole

Yanghan Chen[†], Wei Yi[†,§], Pengcheng Ding[†,‡], Ye Sun[§,]*, Lev Kantorovich[£], and Miao Yu[†,‡,]*

[†]School of Chemistry and Chemical Engineering, Harbin Institute of Technology, Harbin 150001, China

[§]School of Instrumentation Science and Engineering, Harbin Institute of Technology, Harbin 150001, China

[‡]School of Materials and Energy, University of Electronic Science and Technology, Chengdu 610000, China

[£]Department of Physics, King's College London, The Strand, London WC2R 2LS, United Kingdom

*Correspondence to: miaoyu_che@hit.edu.cn, sunye@hit.edu.cn

Abstract

Functionalized porphyrins by introducing exotic atoms into their central cavities have significant applications across various fields. As unique nanographenes, porphyrins functionalized with monoboron are intriguing, yet their synthesis remains highly challenging. Herein, we present the first on-surface boronation of porphyrin, bonding a single boron atom into the porphyrin's cavity. The boronation is selective, being observed exclusively in molecules featuring a specific aromatic ring-fused structure (ARFS*), not the pristine porphyrin molecule or its other ARFS forms. The boron's bonding geometry is non-centered, transforming the boronated porphyrin into a molecular dipole and imparting a markedly varied electronic structure. Well-ordered two-dimensional dipole arrays are achieved. Upon elevated thermoactivation, intermolecular O−B−O bonds provide robustness and flexibility to the molecular chains. This work demonstrates the high selectivity of on-surface porphyrin boronation and provides an effective strategy for tailoring molecules' electronic structure, producing molecular dipoles, and promoting the robustness and flexibility of molecular chains.

Keywords: on-surface synthesis, selective boronation, functionalized porphyrin, electronic structure, scanning tunneling microscopy

Porphyrins are a family of macromolecular heterocyclic compounds having four pyrrole subunits interconnected by =CH–.[1,2] Their molecular board is composed of highly conjugated macrocycles with 26 π electrons. When an exotic atom is introduced into the macrocycle central cavity, the electronic structure of porphyrins can be substantially altered, making this an effective route for functionalizing porphyrins with diverse physical and chemical properties.[3–7] The coordination of porphyrin macrocycles with metals into metalloporphyrins has sparked considerable interest.[8–12] Functionalized porphyrins have demonstrated great utility in photochemistry, organic photoluminescence, opto-storage, sensing, medicine, and various physiological processes (*e.g.*, photosynthesis).[13–23] Distinct from metallo-porphyrins, porphyrins functionalized with non-metallic elements (NMPs) at their macrocycle central cavity exhibit unique properties that bring up new possibilities in chemistry, materials science, and photoelectronic technologies.[24–26] However, NMP development and comprehension remain scarce.

Boron (B), the only nonmetallic element in the III main group, is widely used in all sorts of chemical synthesis. Given the coordination discrepancies, monoboron-porphyrinoids (mBPs) have shown intriguing photophysical and redox properties that differ from diboron-porphyrinoids (dBPs).[27–30] However, due to the +III oxidation state of B and the large porphyrin cavity relative to the small size of the B atom, it is very difficult to produce mBPs in solution.[27] The boronation of porphyrins mostly introduces two B atoms together with other elements, *e.g.*, oxygen (O), to the central cavity, resulting in a steric molecular board with the B or/and O atoms sticking out.[31–33] On-surface synthesis has evolved into a fascinating approach for producing organic compounds that would otherwise be impossible to synthesize in solution or gas.[34–36] So far, there has been no precedent of on-surface boronation yet.

Herein, we report on-surface boronation of porphyrin on Ag(111) (**Scheme 1**). The precursor, 5,10,15,20-tetrakis(4-hydroxyphenyl) porphyrin ($C_{44}H_{30}N_4O_4$, H$_2$THPP), is a tetraphenyl-porphyrin with a hydroxyl group on each phenyl. Combining scanning tunneling microscopy and spectroscopy (STM

and STS) with density functional theory (DFT) calculations, we demonstrate that the boronation is highly selective: only the molecules with a specific aromatic ring-fused structure (ARFS*, which has the largest population among all ARFS forms) have an appropriate covalent bonding environment for B, while no boronation is observed on the pristine H_2THPP or other ARFS forms. *In situ* deposition of B atoms inserts a single B atom into the ARFS* macrocycle cavity, where B adopts a non-centered bonding geometry. The boronation alters the molecular electronic structure significantly and turns the molecule into a molecular dipole. Well-ordered two-dimensional arrays made up of molecular dipoles are achieved. Upon elevated thermal activation, through O–B–O bonds, the boronated ARFS* (B-ARFS*) can form robust and flexible single chains that have never been observed without B.
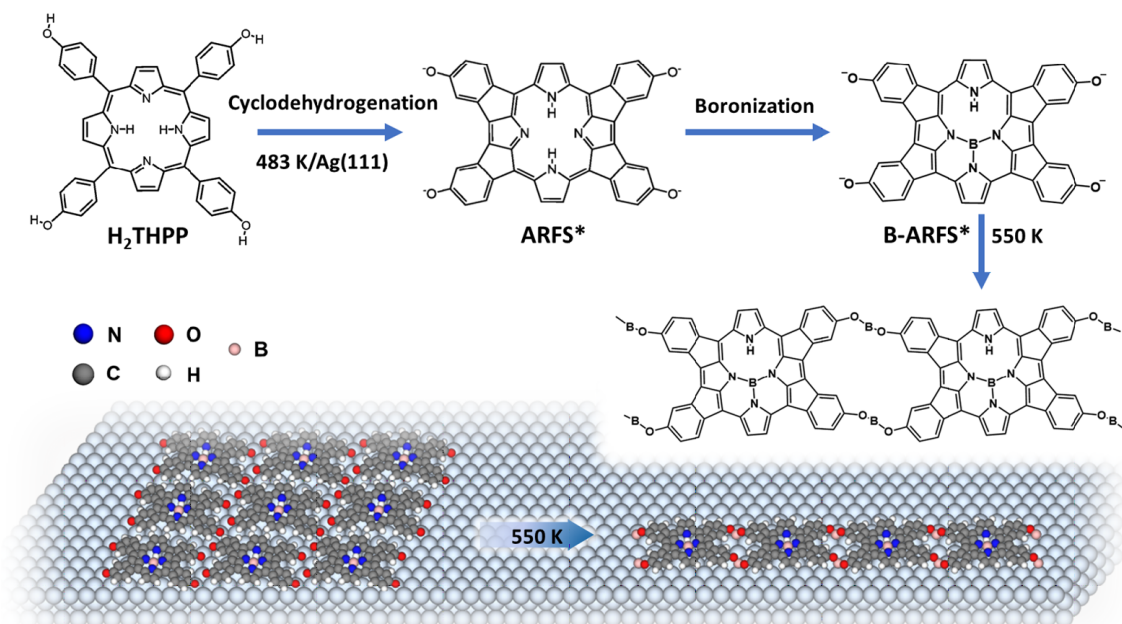
Scheme 1. Schematic illustration of porphyrin boronation on Ag(111). ARFS* is evolved from the H_2THPP precursor *via* cyclodehydrogenation. When evaporating B at 2200 K onto the sample held at room temperature, highly selective boronation of ARFS* is achieved; it does not occur on pristine H_2THPP or other forms of ARFSs. For each boronated ARFS*, *i.e.*, B-ARFS*, a single B is covalently bonded to three N atoms in a non-centered geometry in the porphyrin cavity, converting the porphyrin into a molecular dipole. Well-ordered 2D dipole arrays are achieved. Upon higher thermal activation, B-ARFS* can form single chains through O–B–O bonds, showing high robustness and flexibility. The B, O, N, C, and H atoms are colored pink, red, blue, grey, and white, respectively.

When sublimating H_2THPP molecules from a low-temperature evaporator (450 K) onto a clean Ag(111) surface held at room temperature, closed-packed domains tiled by H_2THPP tetrads are self-assembled on the surface after a post-annealing at 330 K for 20 min (**Figure 1a**). At a positive bias, each molecule is imaged as a pair of parallel baguette-shaped motifs, which is attributed to its saddle-shaped configuration according to the density functional theory (DFT) calculations (**Figure 1b**). The four molecules in each tetrad are rotated by 90° one by one, with two of them aligned along the [11-2] direction and the other two along the [1-10] direction. The periodicities of the two-dimensional (2D) domains are $|a|= 29.6 \pm 0.3$ Å and $|b|= 35.0 \pm 0.3$ Å, with an angle of $\sim 62.7°$ between the two vectors. At the applied annealing temperature, the hydroxyl groups at the H_2THPP corners are partially dehydrogenated,[37] and the molecules interact essentially *via* O–H···O bonds (**Figure S1**).

Further raising the annealing temperature to 483 K, the aryl and macrocyclic pyrrole undergo cyclodehydrogenation, inducing the fusion of aromatic rings. As a result, four distinct ARFSs are produced (**Figure S2**), where ARFS*, containing two 5H-diindeno[2,1-b:1',2'-d]pyrrole-2,10-bis(olate) and two 2,5-dihydro-1H-pyrrole groups, has the highest population (>75%). This is attributed to the favorable formation energy of ARFS* compared with the other three forms (**Figure S3**). ARFS* molecules assemble into well-defined extended 2D domains (**Figures 1c and 1d**), with the periodicities $|a|= 15.0 \pm 0.2$ Å and $|b|= 16.5 \pm 0.2$ Å and an angle of $\sim 48.2°$ between the vectors. The thermal excitation applied (483 K) has been sufficient for a complete hydroxyl dehydrogenation.[37] The O• radicals can interact with the substrate Ag to bend the ARFS corners slightly towards the substrate (**Figure 1e**). The calculated STM image (**Figure 1f**) shows the consistent molecular morphology and arrangement in good agreement with the experimental observations. The charge-density-difference plot (**Figure 1g**) shows no significant charge transfer between the ARFS* central board and the substrate, while the O• radicals connected with the four phenyl legs display evident O–Ag charge transfer. The electron localization function (ELF) mapping (**Figure 1h**) shows that the electrons of the molecules are

highly localized, indicating weak intermolecular interaction. In addition to the 2D domains, ARFS*

molecules form double chains composed of a pair of parallel molecular rows (**Figure S4**). Although

ARFS-A, -B, and -C are capable to have self-metalation on Ag(111) by picking up one Ag atom in their

central cavity (**Figure S5**), the annealing temperature applied here is much lower than that required for

the metalation; in contrast, ARFS* shows no self-metalation until desorption on Ag(111).[37] Thus, the

center cavity of all the four forms of ARFSs is empty.
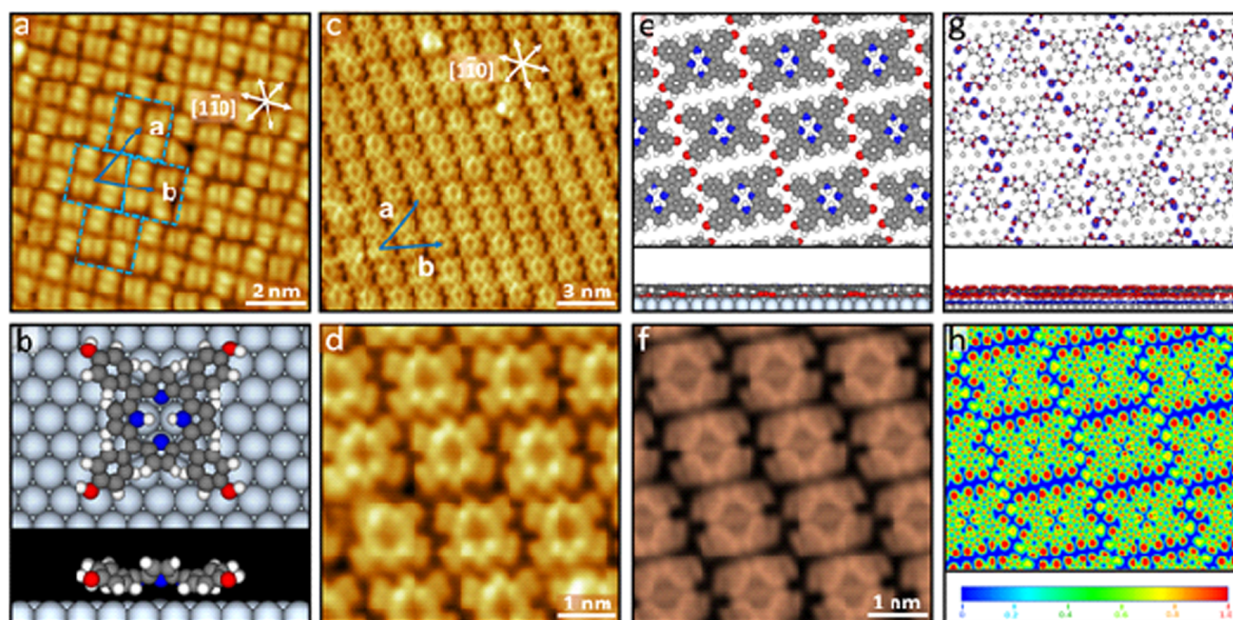
Figure 1. 2D domains of H_2THPP and ARFS* on Ag(111). (a) STM image of close-packed H_2THPP domain on

Ag(111), tiled by molecular tetrads outlined by the blue dashed lines. (b) Top and side views of DFT-calculated model

of a single H_2THPP on Ag(111), showing a saddle-shaped adsorption configuration. (c) Large-scale and (d) close-view

STM images of ARFS* domain obtained after annealing the sample at 483 K. (e) Top and side views of DFT-

calculated structural model, (f) calculated STM image, (g) top and side views of charge density difference plot (the

isovalue is ± 0.002 e/bohr^3; the electron accumulation and depletion are indicated in red and blue, respectively), and (h)

ELF mapping of ARFS* network on Ag(111). 0 and 1.0 in Panel h represent no electron localization and complete

localization, respectively.

When keeping the pristine H_2THPP or ARFSs-covered Ag(111) samples at room temperature and exposing to the elemental B atom flux evaporated at 2200 K, distinct differences are observed. In addition to the emergence of the randomly distributed bright B clusters (which are very mobile compared with the molecules), one additional protrusion corresponding to a single B atom appears in the ARFS* central cavity (**Figures 2a and 2b**), while the 2D order of the domain is practically maintained. In sharp contrast, the central cavities of the pristine H_2THPP or of the other three ARFSs remain empty. The DFT-calculated formation energy of single B with ARFS* cavity on Ag(111) is –4.71 eV, which is significantly stronger than that with H_2THPP (–3.02 eV) or the other three ARFS forms (–2.58, –3.78, and –3.92 eV, respectively). As we scanned the samples at room temperature, we did not see unbonded B monomers or small B clusters on the molecules because they are too mobile to be imaged. Post annealing up to 453 K does not help boronation of ARFS-A, -B, and -C.
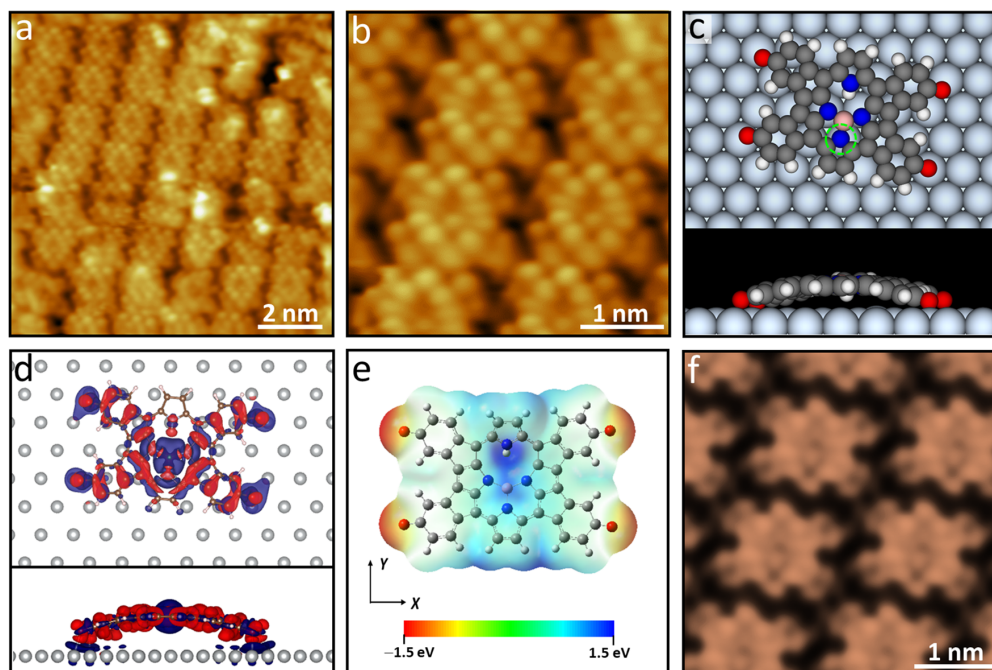
Figure 2. Formation of B-ARFS* on Ag(111). (a) Large-scale and (b) close-view STM images of B-ARFS* on Ag(111). (c) Top and side views of DFT-calculated model and (d) charge density difference plot (isovalue of ±0.002 e/bohr^3) of a single B-ARFS* on Ag(111). (e) DFT-calculated electrostatic potential of a single B-ARFS* colored on the *van der Waals* surface (ρ = 0.0004 a.u.). (f) Calculated STM image of B-ARFS* network on Ag(111).

Remarkably, unlike the case of reported porphyrin metalation,[8-12] the single B is not located at the cavity center of ARFS*, but shifts to one side. According to the DFT-calculated results (**Figure 2c**), the N–H group (circled in green) is deprotonated when bonded with B; the B atom is located at the center of the triangle defined by the three N, and bonded with them at nearly equal bond lengths (1.54 Å). The bonding of the single B atom has to be non-centered: i) the size of B is much smaller than the reported metal atoms for porphyrin metalation and the distance between the two N of N–H groups in the cavity is 4.64 Å, which would be too large to form B–N bonds (with a typical bond length in the range of 1.4–1.6 Å)[38-40] when the B was at the middle point between them; ii) the triangle of the three N provides an appropriate environment to fit B at its III$^+$ state and three strong covalent B–N bonds are formed with significant electron donation from B to N (**Figure 2d**). It is not possible to accommodate two B atoms in the cavity center of ARFS* either; during the structural relaxation, one of the B atoms is thrown out (**Figure S6**).

Interestingly, the B-ARFS* molecules in the same domain have their B located on the same side (**Figures 2a and 2b**). To figure out this origin, we calculated the electrostatic potential of B-ARFS* (**Figure 2e**). The bonded B atom induces intramolecular charge re-distribution, forming a negatively charged region at the B-bonded half and a positively charged opposite section (blue). Such an unbalanced charge distribution of B-ARFS* results in a dipole moment of –1.62 Debye in the y direction (**Figure 2e** and **Table S1**). Due to their high evaporation temperature (2200 K), B atoms have energy to bond with ARFS* at their favorite sites. Based on the intermolecular electrostatic dipole-dipole interaction, fitting the arriving hot B atoms to the same side of B-ARFS* is energetically preferred.

Distinct from the saddle-shaped adsorption of H$_2$THPP, B-ARFS* adopts a center-bulged configuration on the surface, where the B atom is 3.44 Å above the substrate (**Figures 2c and 2d**). As a result, the B only bonds to the three N, but has no charge transfer with the substrate Ag atoms. The calculated STM image (**Figure 2f**) shows a good agreement with the B-ARFS* imaged experimentally. Moreover, B-ARFS* shows markedly varied charge distribution (**Figure 2d**) and electron localization

(**Figure S7**) within the entire molecular board compared with ARFS* (**Figure S8**), indicating the B bonding's impact on the molecular electronic structure.

To explore the B bonding on the molecular electronic structure, we recorded the dI/dV tunneling spectra for ARFS* and B-ARFS*, respectively. The dI/dV spectra are scaled according to their original local density of states (LDOS). Prior to boronation, the black curve collected from the cavity center of ARFS* exhibits (**Figures 3a and 3b**) a wide energy gap near the Fermi level (E_f that is set at 0.0), showing the resonance peaks at –1.10 and +0.67 V, which are attributed to the highest occupied molecular orbital (HOMO) and the lowest unoccupied molecular orbital (LUMO) of ARFS*, respectively. According to the calculated DOS of ARFS* (**Figure 3c**), the HOMO is located at –1.09 V and the LUMO is located at +0.71 V. The calculated HOMO-LUMO gap is 1.80 eV (**Figures 3c and 3d**), which aligns well with the experimentally measured gap (1.77 eV). After boronation, the curve collected from the bonded B in the B-ARFS* (**Figures 3e and 3f**) shows evident shifts of the resonance peaks from –1.10 to –0.72 V and from +0.67 to +0.86 V, resulting in a reduced band gap of 1.58 eV. The calculated DOS of B-ARFS* (**Figure 3g**) indicates that the HOMO and LUMO are located at –0.67 V and +0.88 V, respectively. The resultant HOMO-LUMO gap (**Figures 3g and 3h**) is consistent with the experimental results (1.55 eV *vs.* 1.58 eV). The curve profile changes from flat to parabolic together with multiple minor peaks in the range of –0.6 to –0.7 V and becomes a shoulder on the slope instead of a singular peak in the range of –1.0 to –0.8 V.

Interestingly, besides the cavity's LDOS, the molecular board's LDOS has also evidently altered due to the B bonding. For the spectra from the four corners of ARFS*, they also show a typical semiconductor type profile with the flat curve near E_f, while the resonance peaks above E_f are weaker and the bandgap is narrower than that of ARFS* cavity (**Figures 3a and 3b**). Remarkably, distinct from the corners of ARFS*, the spectra from the B-ARFS* corners show a rather similar profile to its B-bonded cavity in terms of both the profile shape and the resonance peak positions, just the peak intensities are less significant (**Figures 3e and 3f**).
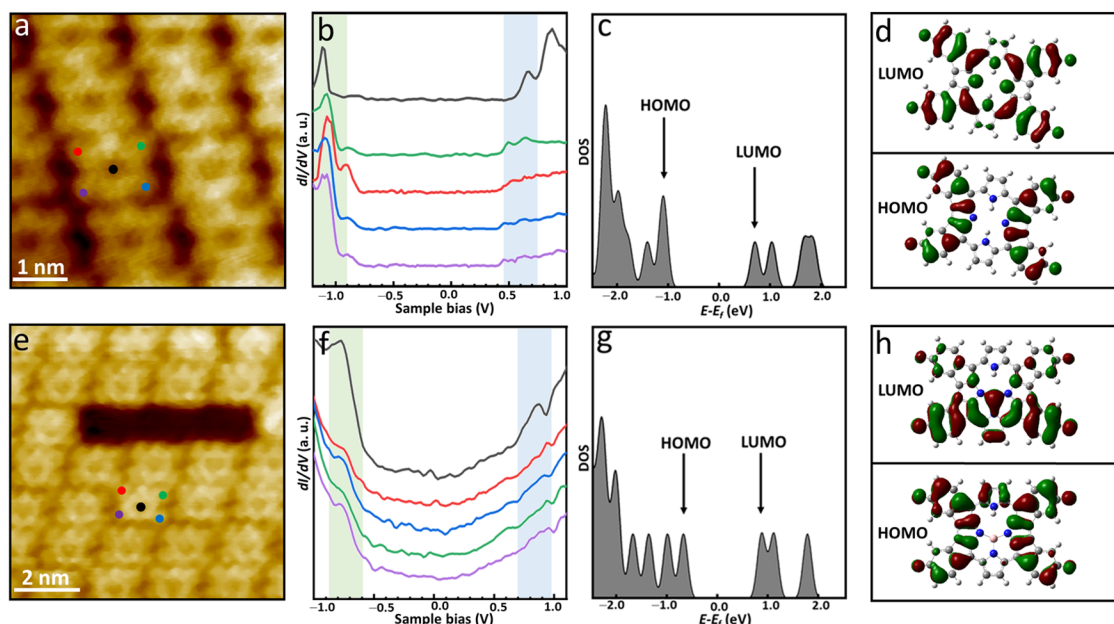
Figure 3. Electronic structure of ARFS* prior to and after boronation. (a) STM image of ARFS* domain on Ag(111) in the absence of B. (b) dI/dV spectra collected from the cavity (black) and four corners of ARFS* (red, purple, green, and blue) as marked in Panel a. (c) DFT-calculated DOS of ARFS*, where the positions of the HOMO and LUMO are indicated by arrows. (d) Calculated LUMO and HOMO of ARFS*. (e) STM image of B-ARFS* domain on Ag(111). (f) dI/dV spectra collected from the cavity (black) and four corners of B-ARFS* (red, purple, green, and blue) as marked in Panel d. (g) DFT-calculated DOS of B-ARFS*, highlighting the HOMO and LUMO positions with arrows. (h) Calculated LUMO and HOMO of B-ARFS*.

When comparing **Figure 3d** with **Figure 3h**, the spatial distribution of the LUMO of ARFS* undergoes pronounced changes upon boronation. Prior to boronation, the LUMO is typically characterized by π orbitals that are delocalized across the entire macrocycle. In contrast, after boronation, as a single B atom bonds with three N atoms within the molecule's central cavity, the LUMO of B-ARFS* becomes more localized around the B atom. This localization stems from the overlap between the B's p-orbitals and the N's lone pairs, resulting in an increased electron density around the B atom and thereby markedly altering the intramolecular charge distribution. Furthermore, the B-induced localization leads to a molecular dipole moment due to the asymmetric distribution of electronic density.

We explored the structural evolution of the boronated surface upon gradually elevated thermal excitation. After annealing at 550 K, the coverage of B-ARFS* is barely reduced, while the 2D molecular domains become less ordered (**Figure S9**). Moreover, singe molecular chains of B-ARFS* emerge on the surface, with the long axis of each molecule deviated by 4.2° from the chain direction (**Figures 4a and 4b**). Such single-chain structure of B-ARFS* is distinct from the double chains of pristine ARFS* (**Figure S4**) and has never been observed in the absence of B. Different from the pristine ARFS* double chains and domains, which are completely desorbed from Ag(111) at 523 K, the single chains remain on the surface at least at 573 K without signs of decomposition or desorption. Moreover, upon STM tip manipulation at room temperature, the double chains of pristine ARFS* are easily broken (**Figures 4c and 4d**); in a sharp contrast, the single B-ARFS* chain can swing like a flexible tail without breaking (**Figures 4e and 4f**). All the results indicate the robust intermolecular bonding, implying the participation of B atoms between neighboring molecules in the formation of this single-chain structure.

Following the STM results, we then constructed the single-chain structural model by placing one B atom beneath each O of the B-ARFS*, so that neighboring molecules share two B atoms (**Figure 4g**). According to the electron difference plot (**Figure 4h**) and ELF mapping (**Figure 4i**), this configuration allows each intermolecular B having significant charge transfer with two O atoms of adjacent B-ARFS* and stabilizing the single chain by O–B–O covalently bonds, meanwhile each B atom can coordinate with the substrate Ag atom underneath to promote the adsorption of the chain on the surface. In this way, the robustness and flexibility of the single chain upon high annealing temperature and STM manipulation are enabled. As the intermolecular B atoms in this case are beneath the molecules and close to the substrate, they are not visible in the experimental and calculated STM images (**Figures 4a, 4b, and 4j**). Another evidence for this structure is that when B atoms are present at the both sides of the chain, the DFT-optimized chain structure is straight (**Figure 4g**); when one side lacks the B atoms, the

chain appears bent (**Figure S10**). This is also consistent with the experimental results (**Figures 4a and 4b**). Additionally, the d*I*/d*V* spectra taken from the B-ARFS* corners in the single chain show more similar curve shape and peak positions to its B-bonded cavity than the B-ARFS* in the 2D domains, further supporting the presence of B atoms on the chain sides.
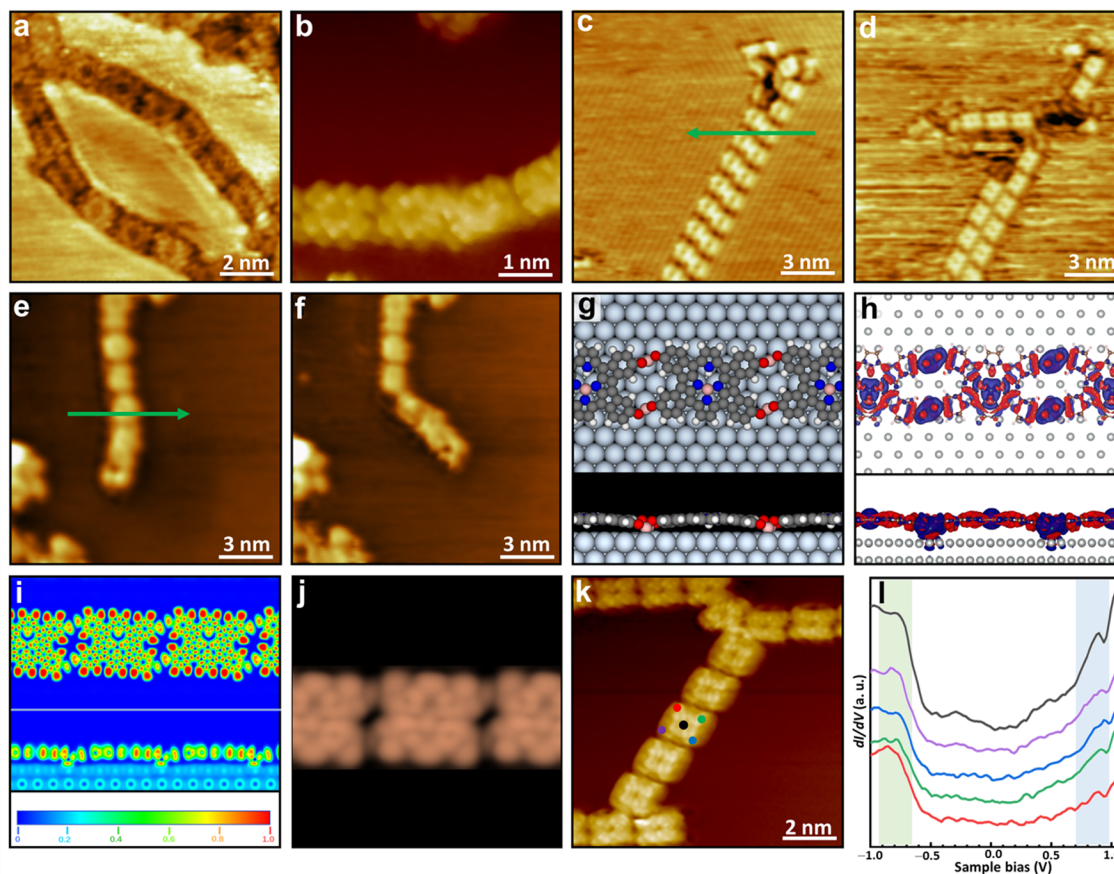

Figure 4. B-ARFS* single chains on Ag(111). (a–b) STM images of the B-ARFS* single chains on Ag(111) after annealing the sampling at 550 K. (c–d) STM manipulation of an ARFS* double chain: when applying the manipulation by STM tip along the direction marked by the green arrow, the double chain is broken easily. (e–f) STM manipulation of a B-ARFS* single chain: when applying the manipulation by STM tip along the direction marked by the green arrow, the single chain shows flexibility to swing like a tail. (g) Top and side views of the DFT-calculated model, (h) charge density difference plot (isovalue of ±0.002 e/bohr^3), (i) ELF mapping, and (j) calculated STM image of the B-ARFS* single chain, with two single B atoms located between neighboring molecules on both sides along the chain. (k) STM image and (l) d*I*/d*V* curves of the B-ARFS* single chain, where the curves in Panel l are collected from different positions marked by the spots of different colors on the B-ARFS* in Panel k.

In summary, on-surface boronation of porphyrin has been realized on Ag(111). A single B atom is covalently bonded in the porphyrin molecule's cavity, resulting in a new monoboron porphyrin compound. The boronation is highly selective, occurring exclusively on ARFS* but not on the porphyrin precursor or its other aromatic-ring-fusing structures. In contrast to metalloporphyrins with the metalation at the porphyrin cavity center, the bonding site of the single B shifts to one side of the cavity, where the triangle of N atoms provides a desirable bonding environment for it. The boronation alters the electronic structure of B-ARFS* and transforms it into a molecular dipole. The B-ARFS* molecules can form single chains *via* O−B−O bonds that are robust and flexible. This work demonstrates the highly selective boronation of porphyrin with single B atoms and provides an effective strategy for tailoring molecules' electronic structure, introducing molecular dipole moments, and enhancing the robustness and flexibility of the molecular chains. The methodology developed here is not limited to porphyrins and may be found useful for other polyaromatic-ring systems.

ASSOCIATED CONTENT

Supporting Information

The Supporting Information is available free of charge on the ACS Publications website at DOI: 10.1021/acs.nanolett.xxxxxxx.

Experimental details, calculation methods, and supplementary figures. (PDF)

AUTHOR INFORMATION

Corresponding Authors

*E-mail: miaoyu_che@hit.edu.cn

*sunye@hit.edu.cn

Notes

The authors declare no competing financial interest.

REFERENCES

(1) Ishizuka, T.; Grover, N.; Kingsbury, C. J.; Kotani, H.; Senge, M. O.; Kojima, T. Nonplanar Porphyrins: Synthesis, Properties, and Unique Functionalities. *Chem. Soc. Rev.* **2022**, *51*, 7560–7630.

(2) Senge, M. O.; Sergeeva, N. N.; Hale, K. J. Classic Highlights in Porphyrin and Porphyrinoid Total Synthesis and Biosynthesis. *Chem. Soc. Rev.* **2021**, *50*, 4730–4789.

(3) Rajasree, S. S.; Li, X.; Deria, P. Physical Properties of Porphyrin-Based Crystalline Metal-Organic Frameworks. *Commun. Chem.* **2021**, *4*, 1–14.

(4) Zhao, L.; Xu, Q.; Shao, Z.; Chen, Y.; Xue, Z.; Li, H.; Zhang, J. Enhanced Oxygen Reduction Reaction Performance Using Intermolecular Forces Coupled with More Exposed Molecular Orbitals of Triphenylamine in Co-Porphyrin Electrocatalysts. *ACS Appl. Mater. Interfaces* **2020**, *12*, 45976–45986.

(5) Ling, Y.; Zhang, Y. Mössbauer, NMR, Geometric, and Electronic Properties in S = 3/2 Iron Porphyrins. *J. Am. Chem. Soc.* **2009**, *131*, 6386–6388.

(6) Chen, Y.; Jiang, D.; Zhang, Y.; Yao, S.; Rosei, F.; Zhang, X.; Huang, Z.-H.; Wang, L.-N.; Kang, F. An 'Ice-Melting' Kinetic Control Strategy for Highly Photocatalytic Organic Nanocrystals. *J. Mater. Chem. A* **2020**, *8*, 25275–25282.

(7) Liu, B.; Miao, G.; Zhong, W.; Huang, X.; Su, N.; Guo, J.; Wang, W. Manipulating the electronic and magnetic properties of coordinated nickel atoms in metal-organic frameworks by hydrogenation. *ACS Nano* **2022**, *16*, 2147–2153.

(8) Wang, Y.; Ogasahara, K.; Tomihama, D.; Mysliborski, R.; Ishida, M.; Hong, Y.; Notsuka, Y.; Yamaoka, Y.; Murayama, T.; Muranaka, A.; Uchiyama, M.; Mori, S.; Yasutake, Y.; Fukatsu, S.; Kim, D.; Furuta, H. Near-Infrared-III-Absorbing and -Emitting Dyes: Energy-Gap Engineering of Expanded Porphyrinoids *via* Metallation. *Angew. Chem. Int. Ed.* **2020**, *132*, 16295–16300.

(9) Wang, J.; Zhong, Y.; Wang, L.; Zhang, N.; Cao, R.; Bian, K.; Alarid, L.; Haddad, R. E.; Bai, F.; Fan, H. Morphology-Controlled Synthesis and Metalation of Porphyrin Nanoparticles with Enhanced Photocatalytic Performance. Nano Lett. **2016**, *16*, 6523–6528.

(10) Goldoni, A.; Pignedoli, C. A.; Di Santo, G.; Castellarin-Cudia, C.; Magnano, E.; Bondino, F.; Verdini, A.; Passerone, D. Room Temperature Metalation of 2H-TPP Monolayer on Iron and Nickel Surfaces by Picking up Substrate Metal Atoms. *ACS Nano* **2012**, *6*, 10800–10807.

(11) Armillotta, F.; D'Incecco, E.; Corva, M.; Stredansky, M.; Gallet, J.-J.; Bournel, F.; Goldoni, A.; Morgante, A.; Vesselli, E.; Verdini, A. Self-Metalation of Porphyrins at the Solid-Gas Interface. *Angew. Chem. Int. Ed.* **2021**, *60*, 25988–25993.

(12) Lepper, M.; Köbl, J.; Zhang, L.; Meusel, M.; Hölzel, H.; Lungerich, D.; Jux, N.; de Siervo, A.; Meyer, B.; Steinrück, H.-P.; Marbach, H. Controlling the Self-Metalation Rate of Tetraphenylporphyrins on Cu(111) *via* Cyano Functionalization. *Angew. Chem. Int. Ed.* **2018**, *57*, 10074–10079.

(13) Sekhar, A. R.; Chitose, Y.; Janoš, J.; Dangoor, S. I.; Ramundo, A.; Satchi-Fainaro, R.; Slavíček, P.; Klán, P.; Weinstain, R. Porphyrin as a Versatile Visible-Light-Activatable Organic/Metal Hybrid Photoremovable Protecting Group. *Nat. Commun.* **2022**, *13*, 3614.

(14) Arellano, L. M.; Gobeze, H. B.; Gómez-Escalonilla, M. J.; Fierro, J. L. G.; D'Souza, F.; Langa, F. Triplet Photosensitizer-Nanotube Conjugates: Synthesis, Characterization and Photochemistry of Charge Stabilizing, Palladium Porphyrin/Carbon Nanotube Conjugates. *Nanoscale* **2020**, *12*, 9890–9898.

(15) Zorlu, Y.; Wagner, L.; Tholen, P.; Ayhan, M. M.; Bayraktar, C.; Hanna, G.; Yazaydin, A. O.; Yavuzçetin, Ö.; Yücesan, G. Electrically Conductive Photoluminescent Porphyrin Phosphonate Metal-Organic Frameworks. *Adv. Opt. Mater.* **2022**, *10*, 2200213.

(16) Min Park, J.; Lee, J. H.; Jang, W.-D. Applications of Porphyrins in Emerging Energy Conversion Technologies. *Coord. Chem. Rev.* **2020**, *407*, 213157.

(17) Xiu, Y.; Zhang, X.; Feng, Y.; Wei, R.; Wang, S.; Xia, Y.; Cao, M.; Wang, S. Peptide-Mediated Porphyrin Based Hierarchical Complexes for Light-to-Chemical Conversion. *Nanoscale* **2020**, *12*, 15201–15208.

(18) Chen, J.; Zhu, Y.; Kaskel, S. Porphyrin-Based Metal-Organic Frameworks for Biomedical Applications. *Angew. Chem. Int. Ed.* **2021**, *60*, 5010–5035.

(19) Jin, Z.; Zhao, P.; Gong, W.; Ding, W.; He, Q. Fe-Porphyrin: A Redox-Related Biosensor of Hydrogen Molecule. *Nano Res.* **2023**, *16*, 2020–2025.

(20) Shi, Y.; Zhang, F.; Linhardt, R. J. Porphyrin-Based Compounds and Their Applications in Materials and Medicine. *Dyes Pigments* **2021**, *188*, 109136.

(21) Yang, F.; Xu, M.; Chen, X.; Luo, Y. Spotlight on Porphyrins: Classifications, Mechanisms and Medical Applications. *Biomed. Pharmacother.* **2023**, *164*, 114933.

(22) Zarrabi, N.; Poddutoori, P. K. Aluminum(III) Porphyrin: A Unique Building Block for Artificial Photosynthetic Systems. *Coord. Chem. Rev.* **2021**, *429*, 213561.

(23) Das, R.; Verma, P. K.; Nagaraja, C. Design of Porphyrin-Based Frameworks for Artificial Photosynthesis and Environmental Remediation: Recent Progress and Future Prospects. *Coord. Chem. Rev.* **2024**, *514*, 215944.

(24) Baklanov, A.; Garnica, M.; Robert, A.; Bocquet, M.-L.; Seufert, K.; Küchle, J. T.; Ryan, P. T. P.; Haag, F.; Kakavandi, R.; Allegretti, F.; Auwärter, W. On-Surface Synthesis of Nonmetal Porphyrins. *J. Am. Chem. Soc.* **2020**, *142*, 1871−1881.

(25) Remello, S. N.; Hirano, T.; Kuttassery, F.; Nabetani, Y.; Yamamoto, D.; Onuki, S.; Tachibana, H.; Inoue, H. Visible Light Induced Oxygenation of Alkenes with Water Sensitized by Silicon-Porphyrins with the Second Most Earth-Abundant Element. *J. Photochem. Photobiol. Chem.* **2015**, *313*, 176−183.

(26) Hussein, B. A.; Shakeel, Z.; Turley, A. T.; Bismillah, A. N.; Wolfstadt, K. M.; Pia, J. E.; Pilkington, M.; McGonigal, P. R.; Adler, M. J. Control of Porphyrin Planarity and Aggregation by Covalent Capping: Bissilyloxy Porphyrin Silanes. *Inorg. Chem.* **2020**, *59*, 13533−13541.

(27) Sinha, A.; Chatterjee, T.; Ravikanth, M. Synthesis and Properties of Boron Porphyrinoids. *Coord. Chem. Rev.* **2022**, *465*, 214574.

(28) Laxman, K.; Reddy, B. P. K.; Mishra, S. K.; Gopal, M. B.; Robinson, A.; De, A.; Srivastava, R.; Ravikanth, M. BF2-Oxasmaragdyrin Nanoparticles: A Non-Toxic, Photostable, Enhanced Non-Radiative Decay-Assisted Efficient Photothermal Cancer Theragnostic Agent. *ACS Appl. Mater. Interfaces* **2020**, *12*, 52329−52342.

(29) Burtsev, I. D.; Dubinina, T. V.; Egorov, A. E.; Kostyukov, A. A.; Shibaeva, A. V.; Agranat, A. S.; Ivanova, M. M.; Sizov, L. R.; Filatova, N. V.; Rybkin, A. Y.; Varakina, E. V.; Bunev, A. S.; Antonets, A. A.; Milaeva, E. R.;

Kuzmin, V. A. Substituted Boron Subphthalocyanines-Prospective Compounds for Theranostics: Synthesis, Photochemical Properties and in Vitro Cytotoxicity. *Dyes Pigments* **2022**, *207*, 110690.

(30) Li, Z.; Gong, Q.; Hao, E.; Jiao, L. B(III)-Subporphyrazines, B(III)-Subporphyrins and Their Hybrids. *Coord. Chem. Rev.* **2023**, *493*, 215325.

(31) Brothers, P. J. Boron Complexes of Porphyrins and Related Polypyrrole Ligands: Unexpected Chemistry for Both Boron and the Porphyrin. *Chem. Commun.* **2008**, *18*, 2090–2102.

(32) Brothers, P. J. Boron Complexes of Pyrrolyl Ligands. *Inorg. Chem.* **2011**, *50*, 12374–12386.

(33) Xu, N.; Ono, T.; Morita, Y.; Komatsu, T.; Hisaeda, Y. Rectangular Holes in Porphyrin Isomers Act As Mono- and Binucleating Ligands: Stereochemistry of Mono- and Diboron Porphycenes and Their Protonation Behaviors. *Inorg. Chem.* **2021**, *60*, 574–583.

(34) Song, S.; Su, J.; Telychko, M.; Li, J.; Li, G.; Li, Y.; Su, C.; Wu, J.; Lu, J. On-Surface Synthesis of Graphene Nanostructures with π-Magnetism. *Chem. Soc. Rev.* **2021**, *50*, 3238–3262.

(35) Mateo, L. M.; Sun, Q.; Liu, S.-X.; Bergkamp, J. J.; Eimre, K.; Pignedoli, C. A.; Ruffieux, P.; Decurtins, S.; Bottari, G.; Fasel, R.; Torres, T. On-Surface Synthesis and Characterization of Triply Fused Porphyrin-Graphene Nanoribbon Hybrids. *Angew. Chem. Int. Ed.* **2020**, *59*, 1334–1339.

(36) Chen, S.; Wang, H.; Ou, Z.; Liu, H.; Zhou, J.; Hu, P.; Wang, Y.; Zhong, D.; Ji, H. On-Surface Synthesis of 2D Porphyrin-Based Covalent Organic Frameworks Using Terminal Alkynes. *Chem. Mater.* **2021**, *33*, 8677–8684.

(37) Chen, Y.; Ding, P.; Sun, Y.; Kantorovich, L. N.; Besenbacher, F.; Yu, M. Highly-Selective Metalation of Porphyrin Enabled by Distinct Aromatic Ring-Fused Structures. *Mater. Today Phys.* **2024**, *42*, 101392.

(38) Mierzwa, G.; Gordon, A. J.; Berski, S. The Nature of Multiple Boron-Nitrogen Bonds Studied Using Electron Localization Function (ELF), Electron Density (AIM), and Natural Bond Orbital (NBO) Methods. *J. Mol. Model.* **2020**, *26*, 136.

(39) Berski, S.; Latajka, Z.; Gordon, A. J. On the Multiple B–N Bonding in Boron Compounds Using the Topological Analysis of Electron Localization Function (ELF). *New J. Chem.* **2011**, *35*, 89-96.

(40) Chen, X.; Tan, D.; Yang, D.-T. Multiple-Boron-Nitrogen (Multi-BN) Doped π-Conjugated Systems for Optoelectronics. *J. Mater. Chem. C* **2022**, *10*, 13499–13532.

TOC

ARFS*   Single B Atom   B-ARFS*

On Ag(111)